AGU PUBLICATIONS

JGR

Journal of Geophysical Research: Atmospheres

RESEARCH ARTICLE
10.1002/2016JD025812

Key Points:
- CrIS and VIIRS are spatially aligned together
- CrIS geolocation error is less than 300 m
- A new geolocation assessment method is developed

Correspondence to:
L. Wang,
wlikun@umd.edu

Citation:
Wang, L., B. Zhang, D. Tremblay, and Y. Han (2017), Improved scheme for Cross-track Infrared Sounder geolocation assessment and optimization, *J. Geophys. Res. Atmos.*, *122*, 519–536, doi:10.1002/2016JD025812.

Received 19 AUG 2016
Accepted 9 DEC 2016
Accepted article online 14 DEC 2016
Published online 5 JAN 2017

Improved scheme for Cross-track Infrared Sounder geolocation assessment and optimization

Likun Wang[1], Bin Zhang[2], Denis Tremblay[3], and Yong Han[4]

[1]Earth System Science Interdisciplinary Center, University of Maryland, College Park, Maryland, USA, [2]Earth Resource Technology Inc., Laurel, Maryland, USA, [3]Science Data Processing Inc., Laurel, Maryland, USA, [4]Center for Satellite Applications and Research/NESDIS/NOAA, College Park, Maryland, USA

Abstract An improved scheme for Cross-track Infrared Sounder (CrIS) geolocation assessment for all scan angles (from −48.5° to 48.5°) is developed in this study. The method uses spatially collocated radiance measurements from the Visible Infrared Imaging Radiometer Suite (VIIRS) image band I5 to evaluate the geolocation performance of the CrIS Sensor Data Records (SDR) by taking advantage of its high spatial resolution (375 m at nadir) and accurate geolocation. The basic idea is to perturb CrIS line-of-sight vectors along the in-track and cross-track directions to find a position where CrIS and VIIRS data matches more closely. The perturbation angles at this best matched position are then used to evaluate the CrIS geolocation accuracy. More importantly, the new method is capable of performing postlaunch on-orbit geometric calibration by optimizing mapping angle parameters based on the assessment results and thus can be further extended to the following CrIS sensors on new satellites. Finally, the proposed method is employed to evaluate the CrIS geolocation accuracy on current Suomi National Polar-orbiting Partnership satellite. The error characteristics are revealed along the scan positions in the in-track and cross-track directions. It is found that there are relatively large errors (~4 km) in the cross-track direction close to the end of scan positions. With newly updated mapping angles, the geolocation accuracy is greatly improved for all scan positions (less than 0.3 km). This makes CrIS and VIIRS spatially align together and thus benefits the application that needs combination of CrIS and VIIRS measurements and products.

1. Introduction

The Cross-track Infrared Sounder (CrIS) is a Fourier transform spectrometer, providing sounding information of the atmosphere with 1305 spectral channels with normal spectral resolution over 3 wavelength ranges: long-wave infrared (9.14–15.38 μm), middle-wave IR (5.71–8.26 μm), and short-wave IR (3.92–4.64 μm). CrIS was first launched on Suomi National Polar-orbiting Partnership (SNPP) satellite in October 2011 and will continue to be on board the following Joint Polar Satellite System (JPSS) satellites. The geolocated, radiometrically, and spectrally calibrated radiances with annotated quality indicators from CrIS—the so-called Sensor Data Records (SDRs)—are used not only to retrieve atmospheric temperature and humidity profiles [e.g., *Divakarla et al*., 2014; *Nalli et al*., 2013] and trace gases [e.g., *Shephard and Cady-Pereira*, 2015] but more importantly to be directly assimilated into numerical weather prediction models as inputs [e.g., *Eresmaa et al*., 2014]. Therefore, the data quality of the CrIS SDR is essential for these applications.

Intensive postlaunch calibration efforts have been carried out by the CrIS SDR team, focusing on improving postlaunch spectral [*Strow et al*., 2013], radiometric [*Tobin et al*., 2013; *Zavyalov et al*., 2013], and geometric calibration [*Wang et al*., 2013] accuracy of CrIS SDR data. Among them, the geometric calibration—which is to accurately map CrIS line-of-sight (LOS) pointing vectors from the detectors to the geodetic latitude and longitude on the Earth ellipsoid surface—is one of the important factors that impact CrIS SDR data quality. Given the spatial resolution of CrIS field of view (FOV) of 14.0 km (at nadir), the designed specification for CrIS geometric calibration accuracy is less than 1.5 km throughout the scan, which are from a tenth to a hundredth of the FOV sizes varying with the scan angles. To achieve this goal, two efforts must be made. First, a method that can quantify the accuracy of the CrIS geolocation relative to the truth reference should be developed. Second, once the symmetric errors are found, it is crucial to refine the geometric calibration parameters based on the assessment results. Mainly focused on CrIS geolocation accuracy assessment, *Wang et al*. [2013] used spatially collocated radiance measurements from the Visible Infrared Imaging Radiometer Suite (VIIRS) band I5 to evaluate the geolocation performance of the CrIS SDR by taking advantage of high spatial resolution (375 m at nadir) and accurate geolocation of VIIRS measurements [*Wolfe et al*., 2013]. The basic idea is to

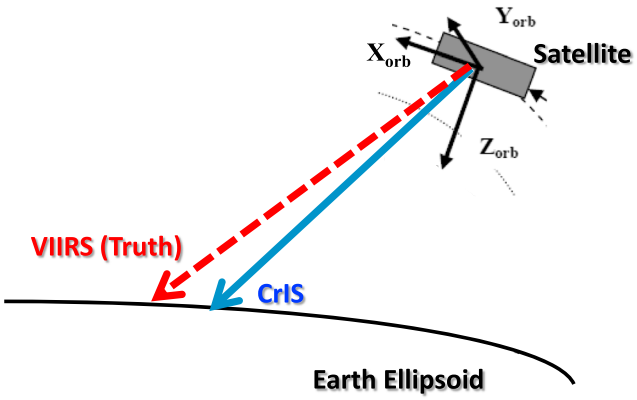

Figure 1. An illustration showing that the goal of geolocation assessment is to identify the error characteristics of LOS pointing vector relative to the truth (VIIRS).

find the best collocation position between VIIRS and CrIS measurements to evaluate the CrIS geolocation performance by assuming the VIIRS geolocation fields as a truth (please refer to section 2.1 on the details of VIIRS geolocation accuracy). Although this study has demonstrated that an intercalibration method of using spatially collocated measurements from VIIRS is effective to quantitatively evaluate geolocation accuracy of CrIS with coarse spatial resolution and spatial gaps among observations, there are still several unresolved issues. First, the method can only evaluate the geolocation accuracy within 30° scan angle. As a result, the evaluation results cannot comprehensively discover error characteristics of CrIS geometric calibration performance. Second, the evaluation results are derived by shifting VIIRS images, which is challenging to diagnose possible errors of CrIS mapping parameters. Third, just like spectral and radiometric calibration, the CrIS geometric calibration parameters should be further adjusted after the satellite was launched. However, it is challengeable to adjust these geometric calibration parameters based on the previous method. This paper improves the method by *Wang et al.* [2013] and presents a better scheme for CrIS geolocation assessment for all scan angles based on CrIS line-of-sight (LOS) vectors. More importantly, the new method is capable of performing postlaunch on-orbit geometric calibration by optimizing mapping angle parameters derived from assessment results and thus can be further extended to the following CrIS sensors on JPSS-1 and JPSS-2.

On the other hand, the combination of high spatial resolution measurements from VIIRS and high spectral resolution measurements from CrIS can take advantage of both spectral and spatial capabilities [e.g., *Li et al.*, 2004]; hence, it can further improve atmospheric and surface geophysical parameter retrievals, data utilization for numerical weather prediction models [e.g., *Eresmaa*, 2014], and intersensor calibration [e.g., *Wang et al.*, 2012]. For these applications, we need to put high spatial VIIRS pixels within CrIS FOVs using their own geolocation data sets, the so-called collocation process [*Wang et al.*, 2016a, 2016b]. However, though onboard the same satellite platform, VIIRS and CrIS are two independent instruments. The geolocation data sets of VIIRS and CrIS are computed separately by their own geolocation algorithms with their own geometric calibration parameters (e.g., instrument internal mapping angles and instrument mounting matrix). In other words, there is no alignment requirement for CrIS and VIIRS. When the data from the two instruments are fused or collocated together, the differences in their geolocation can result in higher uncertainties, especially when CrIS geolocation significantly differs from VIIRS. Therefore, another purpose of this study is to align CrIS observations with VIIRS spatially by resolving their geolocation differences (hereafter, the misalignment between CrIS and VIIRS refers to the significant difference of CrIS geolocation relative to the reference of VIIRS geolocation). Finally, there are ongoing efforts for life-cycle data reprocessing for advancing weather and climate application [*Weng et al.*, 2016]. Once the newly calibrated CrIS geolocation parameters are applied in reprocessing, the improved geolocation accuracy will generate higher-quality CrIS SDR and its downstream products.

The paper is organized as follows: section 2 summarizes the method, section 3 describes the geolocation assessment results, section 4 presents the method of retrieving mapping angle parameters for further geolocation improvements, and section 5 concludes the paper.

2. Method

2.1. Problem Statement

Several issues and considerations on CrIS geolocation evaluation and optimization are explored in this section before the method is discussed in details. The first issue is the main objective of how CrIS geolocation should be quantitatively evaluated. As illustrated in Figure 1, the goal of the CrIS geometric calibration is to accurately

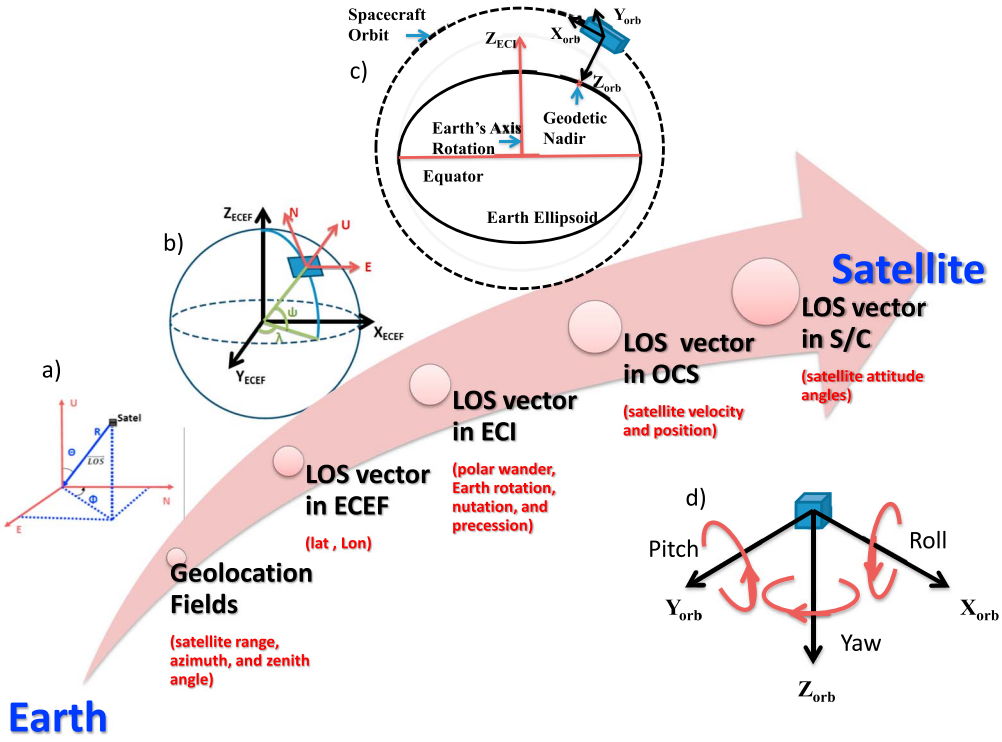

Figure 2. The procedures of inverse geolocation computation to derive the LOS vectors in the Spacecraft Body Frame coordinate system from CrIS geolocation fields. The coordinate systems include (a) Local Spherical coordinate and Local East, North, Up (ENU) coordinate system; (b) Geodetic Latitude, Longitude, and Altitude (LLA) coordinate system and Earth-Centered, Earth-Fixed (ECEF) coordinate system; (c) Earth-Centered Inertial (ECI) coordinate system and Orbital Coordinate System (OCS) coordinate system; and (d) Spacecraft Body Frame (SBF) coordinate system.

map satellite sensor LOS pointing vectors to geodetic longitude and latitude at each FOV for each scan position on the Earth ellipsoid. For each scan, CrIS stepwise "stares" at the Earth step by step in the cross-track direction from −48.3° to +48.3° with a 3.3° step angle, collecting 30 fields of regards (FORs) of the Earth scenes. In each FOR, nine field stops define the 3 × 3 detector array for each wavelength band, which are arrayed as 3 × 3 0.963° circles and separated by 1.1° [see *Han et al.*, 2013, Figure 3]. The aim of geolocation assessment is to identify the error characteristics of LOS pointing vector relative to the truth. It can be achieved by perturbing the CrIS LOS vector at each scan position in both along-track and cross-track directions to find the offset angles that are best matched to the truth. Therefore, the perturbation angles in the along-track and cross-track directions at each scan position can be used to characterize the CrIS LOS vector errors.

The second issue is that in which coordinate system should the CrIS LOS vectors be perturbed? Generally speaking, the CrIS geolocation calculation algorithm is divided into two parts, i.e., the sensor-specific algorithm and the spacecraft-level algorithm. All the instruments on the SNPP and JPSS satellites share the common spacecraft-level algorithm, which computes the intersection of the LOS vectors with the Earth ellipsoid to output geodetic longitude, latitude, and other fields [*Joint Polar Satellite System* (*JPSS*) *Configuration Management Office*, 2011a]. The parameters (e.g., satellite ephemeris and attitude and polar motion data) in the common geolocation part are dynamic (or change with time) and also shared by all the instruments. The sensor-specific algorithm computes CrIS LOS vectors relative to the Spacecraft Body Frame (SBF), which can be found in the CrIS SDR Algorithm Theoretical Basis Document (ATBD) [*JPSS Configuration Management Office*, 2011b]. The mapping angles [see *JPSS Configuration Management Office*, 2011b, Figure 48] at the instrument-level algorithm were measured during the prelaunch test and were set as static values in the ground-processing software. The systematic geolocation errors are mostly caused by the instrument-level parameters due to the uncertainties of prelaunch measurements and other factors on orbit (e.g., satellite launch drift, gravity effects, and thermal distortion). Based on the above practical consideration, the perturbation of CrIS LOS vectors should be carried out at the CrIS instrument level instead of common geolocation part because any changes in the common geolocation part will effect on all the sensors on the same satellite platform.

Table 1. Summary of Coordinate Systems in the Common Geolocation Algorithm

Coordinate Systems	Type	Origin	Variables
Local Spherical coordinate	Spherical	Measurement location	(R, Θ, Φ) R: range (meter) Θ: zenith angle (degree) Φ: azimuth angle (degree)
Local East, North, Up (ENU) coordinate	Cartesian	Measurement location	(east, north, up) in meter
Geodetic Latitude, Longitude, and Altitude (LLA) coordinate	Spherical	Earth center	(ψ, λ, h) ψ: geodetic latitude (degree) λ: longitude (degree) h: altitude (meter)
Earth-Centered, Earth-Fixed (ECEF) coordinate	Cartesian	Earth center	(x, y, z) in meter
Earth-Centered Inertial (ECI) coordinate	Cartesian	Earth center	(x, y, z) in meter
Orbital Coordinate System (OCS) coordinate	Cartesian	Spacecraft center of mass	(x, y, z) in meter
Spacecraft Body Frame (SBF) coordinate	Cartesian	Spacecraft center of mass	(x, y, z) in meter

The third issue is the truth used as a CrIS geolocation assessment reference. For CrIS geolocation assessment, the geolocation fields from VIIRS I bands are used as a truth in this study. The accuracy of VIIRS geolocation has been comprehensively evaluated through the correlation between the Ground Control Point data sets from Landsat and the measurements from VIIRS band 1 [*Wolfe et al*., 2013]. Excluding some anomalies, the mean errors of VIIRS geolocation are about 26 m and 13 m and the root-mean-square errors are about 78 m and 60 m in the in-track and cross-track directions, respectively. Compared to the CrIS coarse resolution (14.0 km at nadir) and relatively low geolocation requirements (1.5 km for all scan positions), VIIRS geolocation is accurate enough and thus can be treated as a truth to evaluate CrIS geolocation accuracy. We have developed a fast and accurate collocation method to collocate CrIS and VIIRS based on LOS pointing vectors in the Earth-Centered, Earth-Fixed (ECEF) coordinate system [*Wang et al*., 2016b]. This method is not only accurate and precise from a mathematical perspective but also easy to implement computationally.

In summary, the whole idea is to produce new sets of CrIS LOS vectors through the perturbation, which are repeatedly collocated with VIIRS LOS vectors. Based on CrIS-VIIRS brightness temperature (BT) differences at each scan position, the best matched CrIS LOS vector can be found.

2.2. Inverse Geolocation Computation

In order to perform the perturbation in the in the SBF coordinate system, we need to perform inverse geolocation computation to derive the CrIS LOS vectors in SBF using CrIS geolocation fields as inputs. These procedures are described in this part, as illustrated in Figure 2. Summarized in Table 1 are all coordinate systems that are used in the common geolocation algorithms. The definition and description of these coordinate systems can be found in the VIIRS Geolocation Algorithm Theoretical Basis Document [*JPSS Configuration Management Office*, 2011a]. The main steps are listed below, including

1. Computing the CrIS LOS vectors in the local East, North, Up (ENU) Cartesian coordinate system using satellite azimuth and zenith angle as well as satellite range (the distance from the FOV center to satellite mass center) for each CrIS FOV;
2. Converting the CrIS LOS vectors from the ENU coordinate system to in the Earth-Centered, Earth-Fixed (ECEF) coordinate system using the geodetic latitude and longitude from each CrIS FOV;
3. Transforming CrIS LOS vectors from ECEF to Earth-Centered Inertial (ECI) using the Naval Observatory Vector Astrometry Software (NOVAS) version 3.1 by doing rotations for wobble (polar wander), spin (Earth rotation), nutation, and precession;
4. Computing the satellite velocity and position vectors in the Earth-Centered Inertial (ECI) coordinate system from the satellite velocity and position vectors in ECEF (that are contained in the geolocation data sets) and building the Orbital Coordinate System (OCS) based on these vectors;
5. Constructing the transformation matrix $T_{ECI2OCS}$ from ECI to OCS and then transforming CrIS LOS vectors from ECI to OCS using the transformation matrix $T_{ECI2OCS}$;
6. Calculating CrIS LOS vectors from OCS to SBF using the satellite attitude angles (roll, pitch, and yaw angles) saved in geolocation data sets.

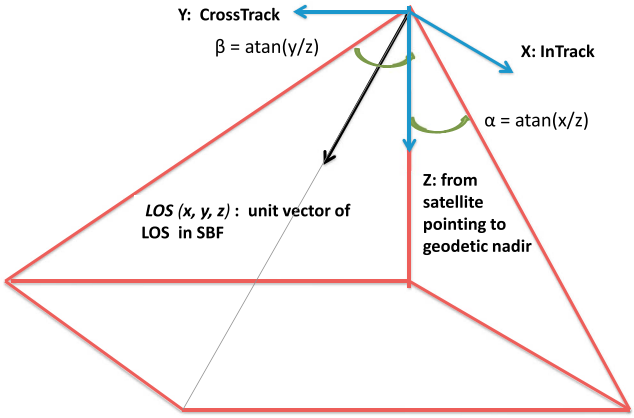

Figure 3. The CrIS LOS vector expressed in the SBF frame, in which two planes are formed, including the in-track (*x*-*z* plane) and cross-track planes (*y*-*z* plane). Two angles of α and β can be simultaneously retrieved, which exactly corresponds to the unit vector of LOS in SBF.

The inputs for the above calculation include geodetic latitude, longitude, satellite range, zenith, and azimuth angles at each CrIS FOV as well as satellite position, velocity, and attitude at each scan, which are saved in CrIS geolocation data set. For computation convenience, the scan-level data are linearly interpolated at the FOV level using the FOV observational time. For more details on the steps 1 and 2 (Figures 2a and 2b), we refer the readers to the study on collocation of CrIS and VIIRS using the LOS vectors in ECEF [*Wang et al.*, 2016b]. The last several steps are discussed below.

2.2.1. Conversion Between ECEF and ECI Frames

ECI frames are called inertial in contrast to the Earth-Centered, Earth-Fixed (ECEF) frame, which rotates in inertial space in order to remain fixed with respect to the surface of the Earth. It is more convenient to represent the CrIS FOV location in the ECEF coordinate system (or with latitude and longitude), but the ECI frame is simple to characterize the satellite orbit in a nonrotating frame (Figure 2c). The conversion between ECEF and ECI are carried out using the Naval Observatory Vector Astrometry Software (NOVAS) version 3.1 [*Bangert et al.*, 2011], which provides community standard transformation between the terrestrial and celestial coordinate systems. The NOVAS function "ter2cel"—which does rotations for wobble (polar wander), spin (Earth rotation), nutation, and precession—is used to transform a vector from the terrestrial to the celestial system. The NOVAS function "cel2ter" does the inverse of tel2cel. An up-to-date Earth orientation parameters can be obtained from the International Earth Rotation Service at ftp://maia.usno.navy.mil/ser7/finals.all, including polar motion values and the time difference in seconds between universal time (UT1; defined by Earth's rotation) and coordinated universal time coordinated (UTC) (defined by a network of precision atomic clocks). The conversion of the velocity between ECEF and ECI requires accounting for the velocity component due to the Earth's rotation in addition to use NOVAS routines. At the same time, the satellite position and velocity in ECEF are converted into the vectors in ECI, which are used to build the OCS frame. The CrIS LOS vectors in ECEF are converted to the ones in ECI for perturbation. After perturbation, the new sets of CrIS LOS vectors are transformed back to ECEF to collocate VIIRS measurements.

2.2.2. Conversion Between ECI and OCS Coordinate Systems

The orbital coordinate system is centered on the satellite, and its orientation is based on the spacecraft position and velocity in inertial space (Figure 2c). The origin is the spacecraft center of mass with the *z* axis pointing from the spacecraft center of mass to the direction perpendicular to the reference ellipsoid (geodetic nadir). The *z* axis can be first derived in ECEF from the satellite position vector in ECEF and then converted back into ECI using the NOVAS software. The *y* axis is the normalized cross product of the *z* axis and the instantaneous satellite (inertial) velocity vector in ECI. The *x* axis is the cross product of the *y* and *z* axes. After these steps, we have all the *x*, *y*, and *z* unit vectors expressed in ECI, which corresponds the vectors of [1, 0, 0], [0, 1, 0], and [0, 0, 1] in OCS. Given two known vectors expressed in the two different coordinate systems, the transformation matrix $T_{ECI2OCS}$ (and its inverse matrix $T_{OCS2ECI}$) between ECI and OCS can be determined using well-known Triad method [*Black*, 1964]. Since the direction of the satellite velocity changed with time, the transformation matrix $T_{ECI2OCS}$ (as well as its inverse matrix $T_{OCS2ECI}$) is also dependent on the FOR position and scan line. With the transformation matrix $T_{ECI2OCS}$, the CrIS LOS vectors can be transformed from ECI to OCS.

2.2.3. Transformation Between OCS and SBF Frames

The orbit frame OCS is a coordinate system describing the perfect attitude of the spacecraft. If the Spacecraft Body Frame (SBF) coordinate system is exactly aligned with the orbit frame, the roll, pitch, and yaw would all be zero and spacecraft attitude would be perfect. In other words, the relationship between the spacecraft and orbital coordinate systems is defined by the spacecraft attitude angles, i.e.,

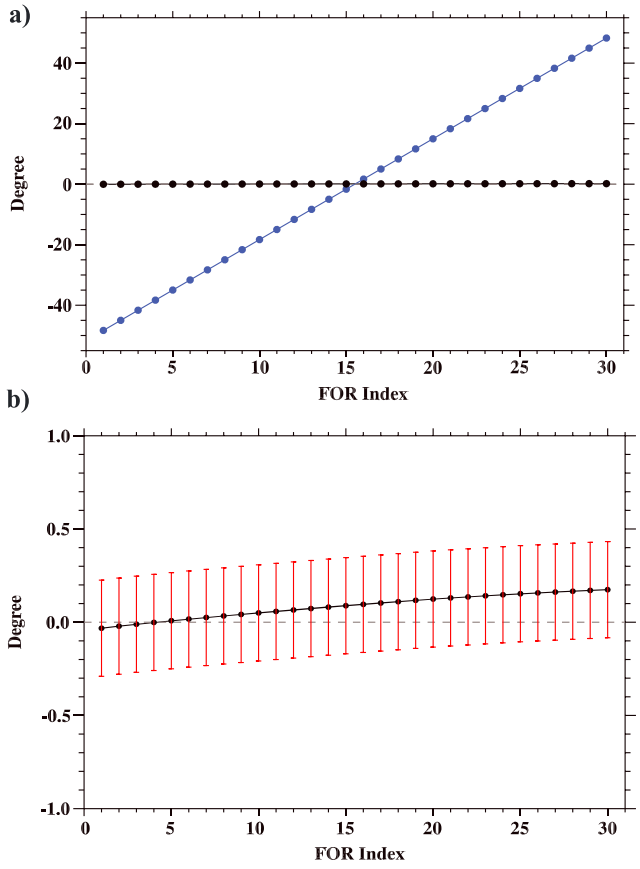

Figure 4. (a) The α (black dots) and β (blue dots) angles varying with scan position for the CrIS center FOV (FOV 5) and (b) enlarged plot of perturbation for α angles varying with the scan position (black dots), where the red bar indicates the perturbation range. Specifically, each red bar gradually increases from the minimum value to the maximum value by 21 steps.

the spacecraft roll, pitch, and yaw angles (Figure 2d), which are saved in geolocation data sets. The transformation from spacecraft to the orbital coordinate system is a three-dimensional rotation matrix with the components of the rotation matrix being functions of the spacecraft roll, pitch, and yaw attitude angles, which follows the order of yaw, roll, and pitch (called type 3-1-2) [see Appendix B of *JPSS Configuration Management Office*, 2011a]. Once the transformation matrix is derived, the CrIS LOS vectors can be transformed from OCS to SBF.

2.3. Perturbation of CrIS LOS Vector in SBF

As shown in Figure 3, after the above transformation, the CrIS LOS vector is expressed in the SBF frame. Basically, two planes are formed in the SBF frame, i.e., the in-track (*x*-*z* plane) and cross-track planes (*y*-*z* plane). Once the unit CrIS LOS vector $\overrightarrow{LOS}$ (*x*, *y*, *z*) is projected onto these two planes, two angles of α and β can be simultaneously retrieved as

$$\alpha = \tan^{-1}\left(\frac{x}{z}\right), \tag{1}$$

$$\beta = \tan^{-1}\left(\frac{y}{z}\right). \tag{2}$$

Specifically, the α angle describes the relative location of CrIS LOS vector $\overrightarrow{LOS}$ in the in-track direction, while the β angle indicates the relative positions of the CrIS LOS vector moving in the cross-track direction. More importantly, the α and β angles exactly correspond to the CrIS LOS vector $\overrightarrow{LOS}$. In other words, if α and β angles change, the direction of the vector $\overrightarrow{LOS}$ also changes. Therefore, it is possible to perturb the CrIS LOS vector $\overrightarrow{LOS}$ by changing α and β angles, which simplifies the perturbation from three variables to two variables. Illustrated in Figure 4a is an example of α and β angles varying with scan position for the CrIS center FOV (FOV 5), which are calculated from CrIS geolocation data fields. It clearly shows that the moving of CrIS LOS vectors is dominated in the cross-track direction because the CrIS scene selection mirror mainly rotates along the cross-track direction. Based on these calculated α and β angles, a total of $2n+1$ ($n=10$ in this study) of new α_i and β_j angles can be computed as

$$\alpha_i = \tan^{-1}\left(\frac{x}{z}\right) + (i-n)\cdot s, \qquad i = 0,\ 1,\ \ldots\ 2n+1, \tag{3}$$

$$\beta_j = \tan^{-1}\left(\frac{y}{z}\right) + (j-n)\cdot s, \qquad j = 0,\ 1,\ \ldots\ 2n+1, \tag{4}$$

where *s* is the perturbation step size and set as 375.0/833000.0 (VIIRS pixel size resolution divided by the satellite altitude). Particularly, in the case of when *i* equals *n*, the values of α_i and β_j are equal to α and β, which are computed in equations (1) and (2). Correspondingly, the offset angles relative to the α and β angles are defined as $\Delta\alpha_i$ and $\Delta\beta_j$ as

$$\Delta\alpha_i = \alpha_i - \alpha_n, \tag{5}$$

$$\Delta\beta_i = \beta_i - \beta_n. \tag{6}$$

Figure 4b gives an enlarged plot of α_i angles varying with the scan position (black dots), where the red bar indicates the perturbation range of α_i at each scan position. In other words, each red bar in Figure 4b gradually increases from the minimum value to the maximum by 21 steps.

Based on α_i and β_j angles, a total of 441 unit vectors $\overrightarrow{LOS}_{i,j}$ in the SBF frame can be derived as

$$\overrightarrow{LOS}_{i,j} = \text{UNIT}\left(\text{ztan}\beta_j, \quad \text{ztan}\alpha_i, \quad \text{z}\right). \tag{7}$$

Among these vectors, $\overrightarrow{LOS}_{i,j}$, the vector $\overrightarrow{LOS}_{10,10}$ is the original vector computed from the original geolocation data, while other 440 vectors are those perturbed along the in-track and cross-track directions.

2.4. Determination of Geolocation Accuracy

The new sets of CrIS vector $\overrightarrow{LOS}_{i,j}$ in the SBF frame are converted back to the ECEF frame from the SBF frame step by step, which are then collocated with the VIIRS pixels using the method by *Wang et al.* [2016b]. When spatially collocating with VIIRS observations, each vector $\overrightarrow{LOS}_{i,j}$ corresponds a spatially averaged VIIRS radiance $R^{\text{VIIRS}}_{i,j}$, which can be further converted into the brightness temperature as $\text{BT}^{\text{VIIRS}}_{i,j}$. On the other hand, CrIS spectra can be integrated with VIIRS spectral response functions and then converted into CrIS-simulated VIIRS BT^{CrIS}. Therefore, for each BT^{CrIS}, there is a total of 441 $\text{BT}^{\text{VIIRS}}_{i,j}$. For any arbitrarily selected inhomogeneous scenes (such as cloudy areas), the standard deviation of CrIS-VIIRS BT differences (i.e., $\text{BT}^{\text{VIIRS}}_{i,j} - \text{BT}^{\text{CrIS}}$ with N samples) is very sensitive to the geolocation mismatch between CrIS and VIIRS, while the mean BT differences are mostly controlled by the radiometric differences between two sensors [*Wang et al.*, 2013]. Therefore, the question of determining CrIS geolocation accuracy is simplified to find which one among 441 $\text{BT}^{\text{VIIRS}}_{i,j}$ is best matched with one CrIS observations. Thus, it is possible to define a cost function G as

$$G\left(\Delta\alpha_i, \quad \Delta\beta_j \ , \ k\right) = \text{STDEV}\left(\text{BT}^{\text{VIIRS}}_{i,j}(k) - \text{BT}^{\text{CrIS}}(k)\right), \tag{8}$$

where $\text{BT}^{\text{VIIRS}}_{i,j}(k)$ and BT^{CrIS} (k) are the two independent variables with N samples and k is the scan position index and varies from 1 to 30 (FOR number). Especially, the cost function G is a three-variable function varying with the offset angles $\Delta\alpha_i$ and $\Delta\beta_j$ as well as the scan position index. We can derive the offset angles $\Delta\alpha_i$ and $\Delta\beta_j$ from the minimum value of the cost function G at each scan position, which characterizes how the original CrIS LOS vectors should be shifted in the cross-track and in-track direction in order to perfectly match the "truth" (VIIRS geolocation fields). It should be noted that the offset angles is relative to the original LOS vector for implementation consideration, the sign of which is different from the often-used error characterization method.

Given in Figure 5 is an example of how to determine the CrIS geolocation accuracy using the defined cost function G. CrIS and VIIRS I5 band granules over the tropical oceans are shown in Figures 5a and 5b, in which clouds are randomly distributed over ocean. Figure 5c shows the contour plot of the defined cost function G varying with the offset angles $\Delta\alpha_i$ and $\Delta\beta_j$ at the FOR 30. The two scatterplots of VIIRS versus CrIS BTs are given in Figure 5d; that is, one is from the position where $\Delta\alpha_i = 0$ and $\Delta\beta_j = 0$ (black dots) and the other from the position where the cost function G is close to the minimum value ($\Delta\alpha_i = -412.3$ μrad and $\Delta\beta_j = 1787.5$ μrad; green dots). The method of how to identify the minimum value from the cost function can be found in the previous study [*Wang et al.*, 2013]. It clearly shows that the spread of the scatterplots of VIIRS BTs versus CrIS BTs greatly decreases (the standard deviation of CrIS-VIIRS BT differences decreases from 0.91 K to 0.22 K), indicating that the actually CrIS LOS vector is located at the position where the cost function G has the minimum value. In other words, one can state that, compared to the VIIRS LOS vector, the CrIS LOS vector should be off about −412.3 μrad in the in-track direction and about 1787.5 μrad in the cross-track direction for the scan position 30.

In brief, the flowchart in Figure 6 summarizes the method on how to determine the CrIS geolocation accuracy using VIIRS image band geolocation fields. The closed cycle indicates the perturbation procedures that generate 21×21 CrIS LOS vectors in the SBF frame. They are then converted back into ECEF and collocated with

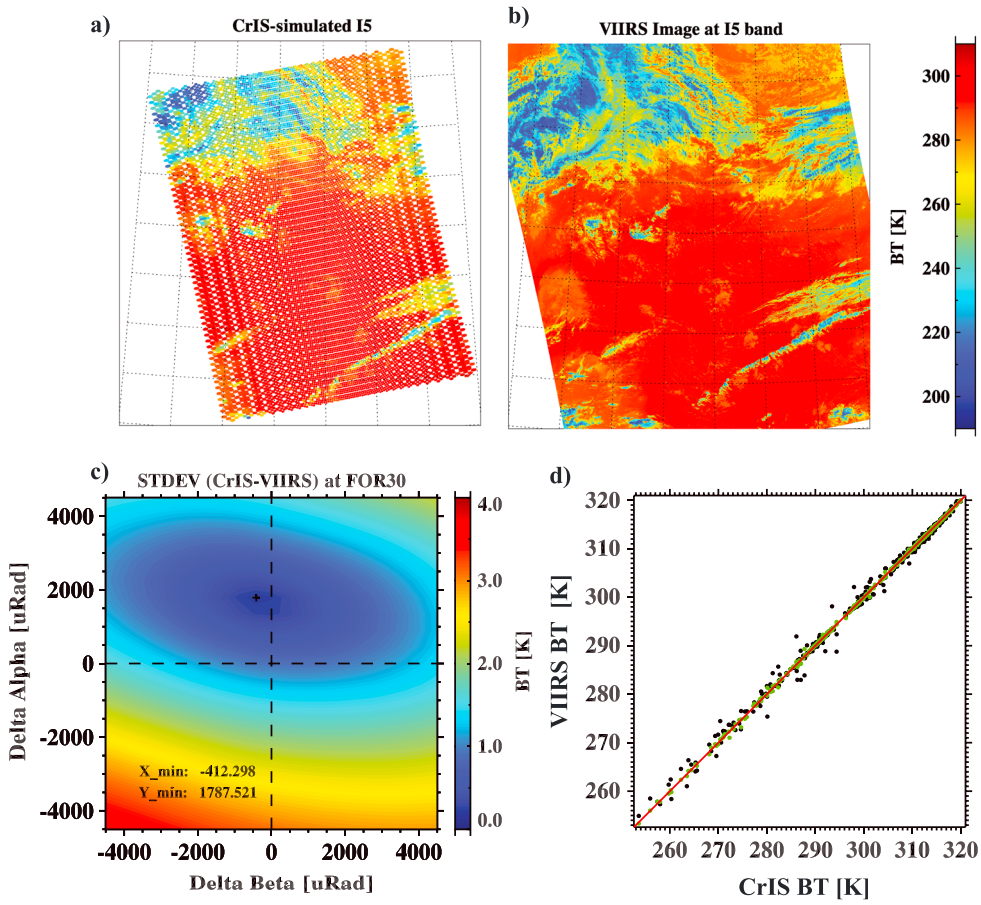

Figure 5. An example illustrating the method to derive the cost function: (a) CrIS-simulated image for VIIRS I5 band, (b) VIIRS image from I5 band, (c) the contour plot of the standard deviation of CrIS-VIIRS BT differences varying with offset angles $\Delta\alpha$ and $\Delta\beta$, and (d) scatterplots of VIIRS and CrIS BTs at the positions of ($\Delta\boldsymbol{\alpha_i} = 0$, $\Delta\boldsymbol{\beta_j} = 0$) indicated by black dots and ($\Delta\boldsymbol{\alpha_i} = -412.3$ μrad, $\Delta\boldsymbol{\beta_j} = 1787.5$ μrad) represented by green dots, in which the standard deviation of BT difference reduces to 0.22 K from 0.91 K.

VIIRS observations in ECEF. The best matched CrIS LOS vectors are identified to correspondingly derive the offset angle $\Delta\alpha_i$ and $\Delta\beta_j$, which basically characterize the CrIS geolocation accuracy.

3. Geolocation Assessment Results

3.1. Assessment Results for Operational CrIS SDR Products

We use the method presented in section 2 to examine CrIS geolocation accuracy for current CrIS SDR operational products, which are generated by the operational ground-based processing software—Interface Data Processing Segment (IDPS). We arbitrarily choose 10 days' data. Without losing generality, the cases include both in an ascending and descending mode, as well as those located in different geographic regions (mid-latitude, polar, and tropical regions). Each case is composed by 14 CrIS granules (4 scans in each granule) with inhomogeneous scenes (e.g., cloudy scenes or land-sea contrast coast regions). For each scan position, there a total of $14 \times 4 \times 9$ samples to derive the statistics. Figure 7 shows the assessment results of the offset angles $\Delta\alpha$ and $\Delta\beta$ identified from the 10 day data, in which the black dots represent the each case's results and the red dots with the error bar gives the statistics including the mean and standard deviation. To make the results easily understandable, the offset angles $\Delta\alpha$ and $\Delta\beta$ can be divided by the FOV size angle of 0.963° (16,807.521 μrad), indicated by the *y* axis on the right in Figure 7. First, the offset angles $\Delta\alpha$ and $\Delta\beta$ results detected from different cases are consistent to each other, suggesting that there are systematic errors in CrIS geolocation computation. Second, the results change with scan positions in the both in-track and cross-track directions. Specifically, as shown in Figure 7b in the cross-track direction, the offset angle $\Delta\beta$ is

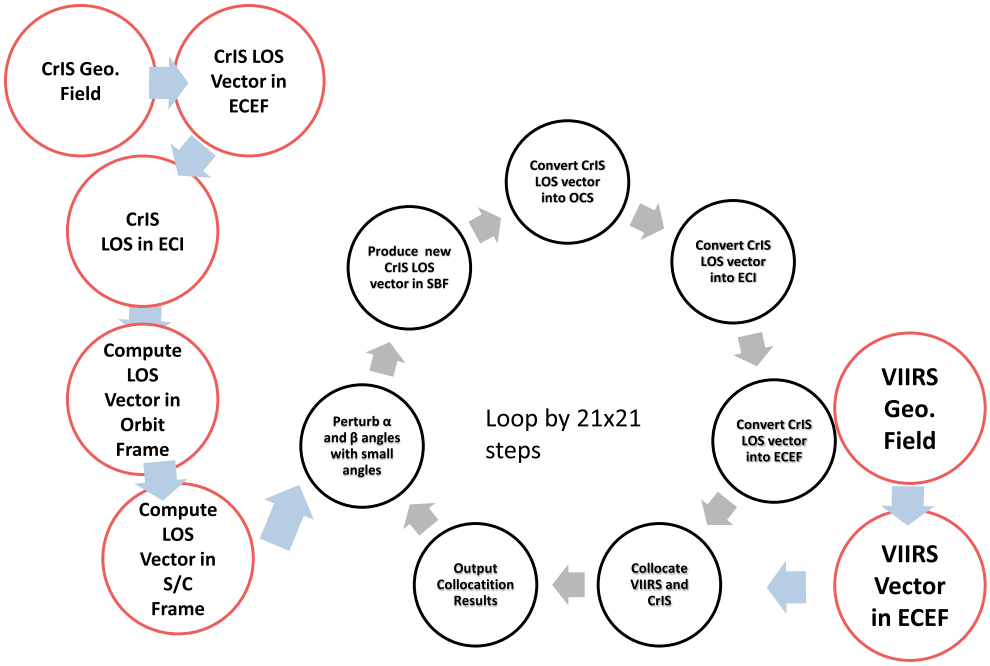

Figure 6. The flowchart summarizing the method of evaluating the CrIS geolocation accuracy using VIIRS image band geolocation fields.

close to zero from scan position 1 to 10; it gradually increases beginning from scan position 10 and finally reaches to 1752 μrad (10.4% of FOV size). On the other hand, in the in-track direction, the offset angle $\Delta\alpha$ changes from the positive values at the beginning of the scan (5.1% of FOV size) to the negative values (−3% of FOV size) at the end of scan, showing a yaw pattern. Based on the statistics, a quadratic curve fit line along the scan position is overlapped as the green lines in Figure 7, which basically characterize error statistics of CrIS geolocation. To make the results straightforward, the angles shown in the fitting line in Figure 7 can be further converted into the distance by using the FOV size varying with scan position [see *Wang et al*., 2013, Figure 15], which are given in Figure 8. Due to the Earth curvature and increasing scan angles, CrIS FOV size exponentially increase in the cross-track direction with scan angles. In other words, the CrIS FOV size at the end of the scan is 3.47 times (~48 km) in the cross-track direction and 1.74 times (24 km) in the track direction compared to the nadir FOV size (14 km). First, compared to the near-nadir results (FOR 7–22) with previous study [*Wang et al*., 2013, Figure 16], the pattern and results agree well except that the sign convention in the in-track direction is opposite. Second, with the new improved method, we have a chance to evaluate the CrIS geolocation accuracy for all scan angles. As shown in Figure 8, the largest geolocation error for CrIS geolocation is located at the end of scan in the cross-track direction, which is larger than 2.0 km from FOR 20 and can finally reach to 4.7 km at the end of scan, while other parts are below 1.5 km. The similar findings were reported by previous study [*Brunel and Roquet*, 2015]. This issue can be clearly demonstrated in Figure 9, showing CrIS and CrIS-VIIRS BT difference images at the Red Sea regions during daytime from three different granules. These three CrIS images passed over the Red Sea around the beginning, the middle, and the end of scan. Since the CrIS-VIIRS BT differences are very sensitive to the spatial mismatch between CrIS and VIIRS over the land-sea contract coast regions, the Red Sea shape is clearly shown at the end of the scan, but it is hard to see in the beginning and middle of the scan. More importantly, the coastline close to nadir shows a cold bias (negative), while the one far away from nadir displays warm bias (positive), suggesting that the mismatch is dominated in the cross-track directions. It agrees with Figures 7 and 8. All the results imply that the CrIS geometric calibration parameters need further adjustment.

3.2. Changes in CrIS Geolocation Computation Software

Before we try to adjust the CrIS geometric calibration parameters, we carefully examined the CrIS geolocation computation software and identified two potential issues. First, the sign convention that defines the FOV

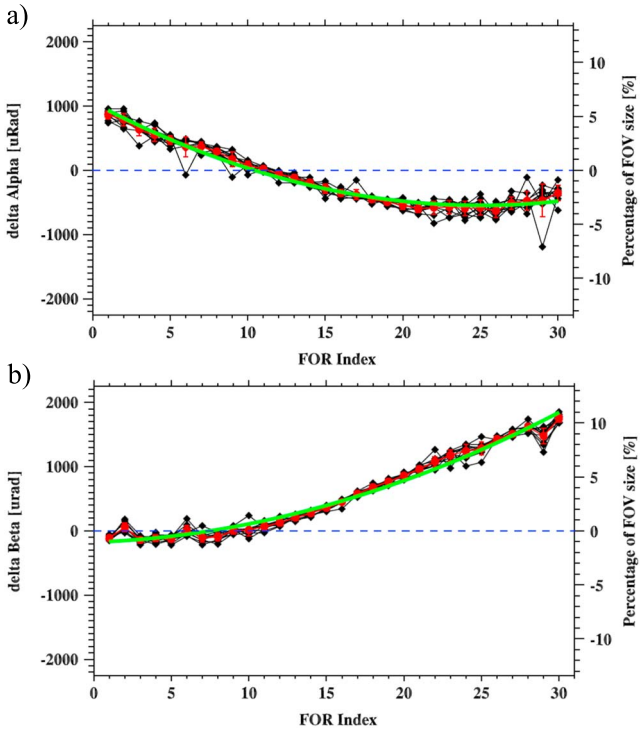

Figure 7. CrIS geolocation assessment results for CrIS IDPS geolocation data sets, including (a) the offset angle $\Delta\alpha$ in the in-track direction and (b) the offset angle $\Delta\beta$ in the cross-track direction, in which the black dots represent the each case's results and the red dots with the error bars that give the statistics including the mean and standard deviation. The green lines indicate the quadratic curve fit line along the scan position. The percentage of offset angles $\Delta\alpha$ and $\Delta\beta$ relative to the FOV size (0.963°) is indicated by the *y* axis on the right.

position angle in the cross-track direction in the Engineer Packets (EP) is not consistent to the convention for numbering FORs and FOVs [see *Han et al.*, 2013, Figure 3; *JPSS Configuration Management Office*, 2013, Figure 143]. In the CrIS sensor specifications, the extent of the FOR is equal in the in-track and cross-track directions (i.e., 3.3°). The FOV footprint size (0.963°) and FOV sampling interval (1.100°) are also equal in the two directions [*Han et al.*, 2013, Figure 3; *JPSS Configuration Management Office*, 2013, Figure 143]. The position of each FOV located in the FOR is defined by the FOV angles in the cross-track and in-track directions relative to the central FOV (FOV 5). If the FOV angle in the cross-track direction is opposite, the side FOVs (FOVs 1 and 3, FOVs 4 and 6, and FOVs 7 and 9) are flipped in the cross-track direction. In order to follow the FOV numbering specifications, the CrIS geolocation computation software has to remap the FOV geolocation fields as well as quality flag of three pairs of corresponding side FOVs. This is not an issue if the central FOV (FOV 5) perfectly aligns with interferometer optical axis, which means that the cross-track and in-track angles of the central FOV are zero. However, in reality, the central FOV cross-track and in-track angles are not zero and have been set as small values (−359 μrad in the cross-track direction and 150 μrad in the in-track direction) during the

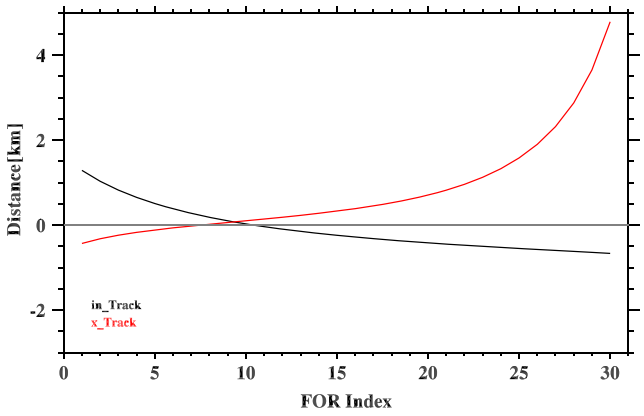

Figure 8. CrIS geolocation assessment results expressed in distance in the in-track (black) and cross-track (red) directions for IDPS CrIS geolocation data sets.

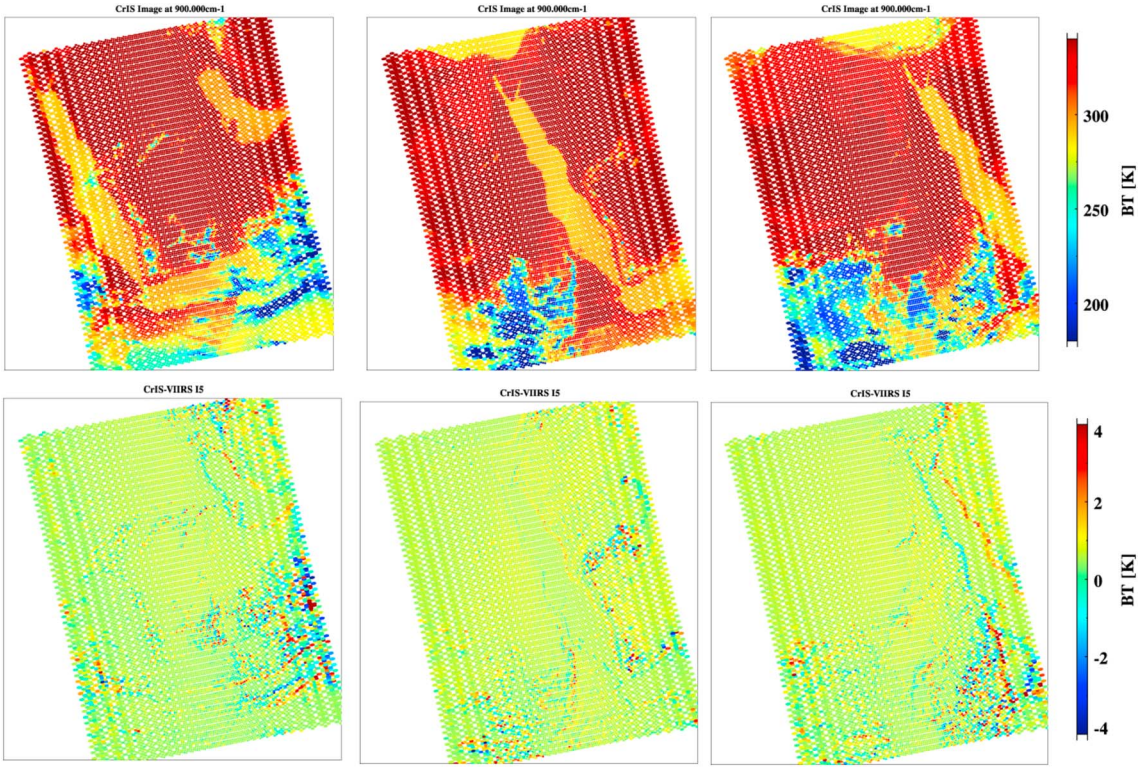

Figure 9. (top) CrIS and (bottom) CrIS-VIIRS BT difference images at the Red Sea regions from three different granules, which clearly shows the land features at the end of CrIS scan due to the misalignment between CrIS and VIIRS.

postlaunch spectral calibration [*Strow et al.*, 2013]. After the discussion with the CrIS SDR team members, the proposed changes include (1) removing the subroutine of remapping FOVs, (2) keeping the same sign of the FOV position angle in the cross-track direction in the EP in order to make the EP consistent for future mission, and (3) reversing the sign the FOV position angle in the cross-track direction when the CrIS geolocation algorithm uses these angles.

Another bug identified in the CrIS geolocation algorithm is that when building the transformation matrix in the two coordinate systems in the internal instrument, the algorithm does not follow the same order as suggested in the CrIS SDR ATBD to use the mapping angle [*JPSS Configuration Management Office*, 2011b]. However, since all the mapping angles in the internal instruments are very small, this bug does not significantly change CrIS geolocation fields.

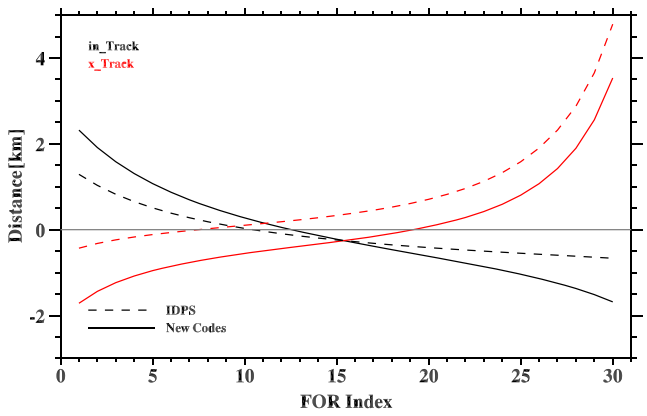

Figure 10. CrIS geolocation assessment results in distance for CrIS-geolocation data sets produced by IDPS (dashed lines) and newly updated ADL software (solid lines).

We implemented these updates in the JPSS Algorithm Development Library (ADL)—a counterpart of IDPS operational software. Using the newly updated software, the new geolocation data sets are regenerated for the selected 10 day data. These newly produced data are then evaluated using collocated VIIRS, and the final results are given in Figure 10. To make it clear, the plots in Figure 8 are also overlapped and shown as the dashed lines. First,

Table 2. Summary of Coordinate Systems in the CrIS Instrument As Well As Their Mapping Angles

Coordinate Systems	Mapping Angles
Interferometer Optical Axis Reference (IOAR)	FOV 5 offset angles in IOAR: two angles (pitch and yaw)
Scene Selection Mirror Mounting Feet Frame (SSMF)	IOAR → SSMF: two angles (pitch and yaw) Normal vector to SSM mirror in SSMF for each scan position: 2 × 30 angles (in-track and cross-track angles)
Scene Selection Module Reference (SSMR)	SSMF → SSMR: three angles (roll, pitch, and yaw)
Instrument Alignment Reference (IAR)	SSMR → IAR: three angles (roll, pitch, and yaw)
Spacecraft Body Frame (SBF)	IAR → SBF[a]: three angles (roll, pitch, and yaw)

[a]These three angles are set as zero in EP but are taken into account in the configuration file of the processing software.

since the sign of the cross-track FOV angle has been reversed, the curve in the cross-track direction is shifted down all the scan position. On the other hand, in the in-track direction, the changes are really complicated. It seems that the previously shown yaw pattern in the in-track direction is even worse. By and large, the new codes cannot remove the geolocation bias revealed by collocated VIIRS data, and thus, we have to further investigate the CrIS mapping angles in order to improve CrIS geolocation accuracy.

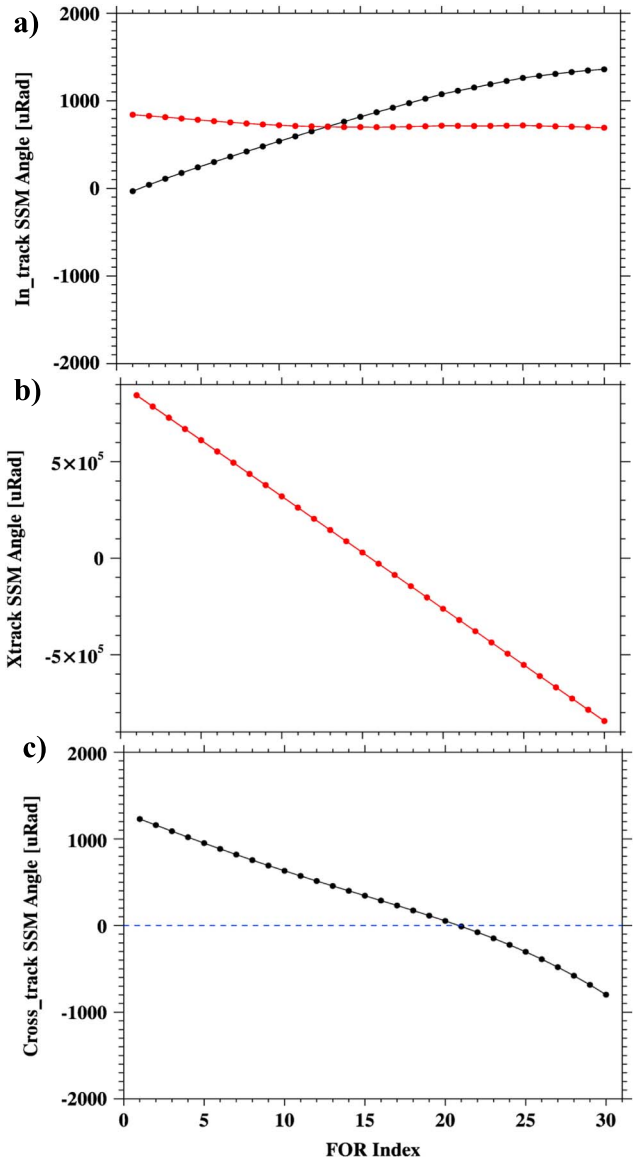

Figure 11. A new set (red) of the SSM (a) in-track and (b) cross-track angles derived from geolocation assessment results, compared with the old values (black). (c) The angle differences in the cross-track direction are given because their values are too close and it is hard to see in Figure 11b.

4. Mapping Angle Parameter Optimization

4.1. Deriving New Mapping Angles

In this section, we discuss the method on how to use assessment results to further adjustment CrIS mapping angles in the instrument level for CrIS geolocation improvements. Since the mapping angles in the internal instrument were measured during the prelaunch test, it is most likely that these parameters are changed due to many factors after launch, such as launch shift, gravity effects, and thermal distortion. Therefore, it is important to perform postlaunch geometric calibration to refine calibration parameters just like the radiometric and spectral calibrations after satellite launch. Table 2 lists the mapping angles and coordinate systems that are used to compute the LOS vector in the CrIS instrument level [see *JPSS Configuration Management Office*, 2011b, Figure 48]. The detailed description on these coordinate systems can be referred to CrIS SDR ATBD [*JPSS Configuration Management Office*, 2011b]. At this stage, we do not have knowledge on

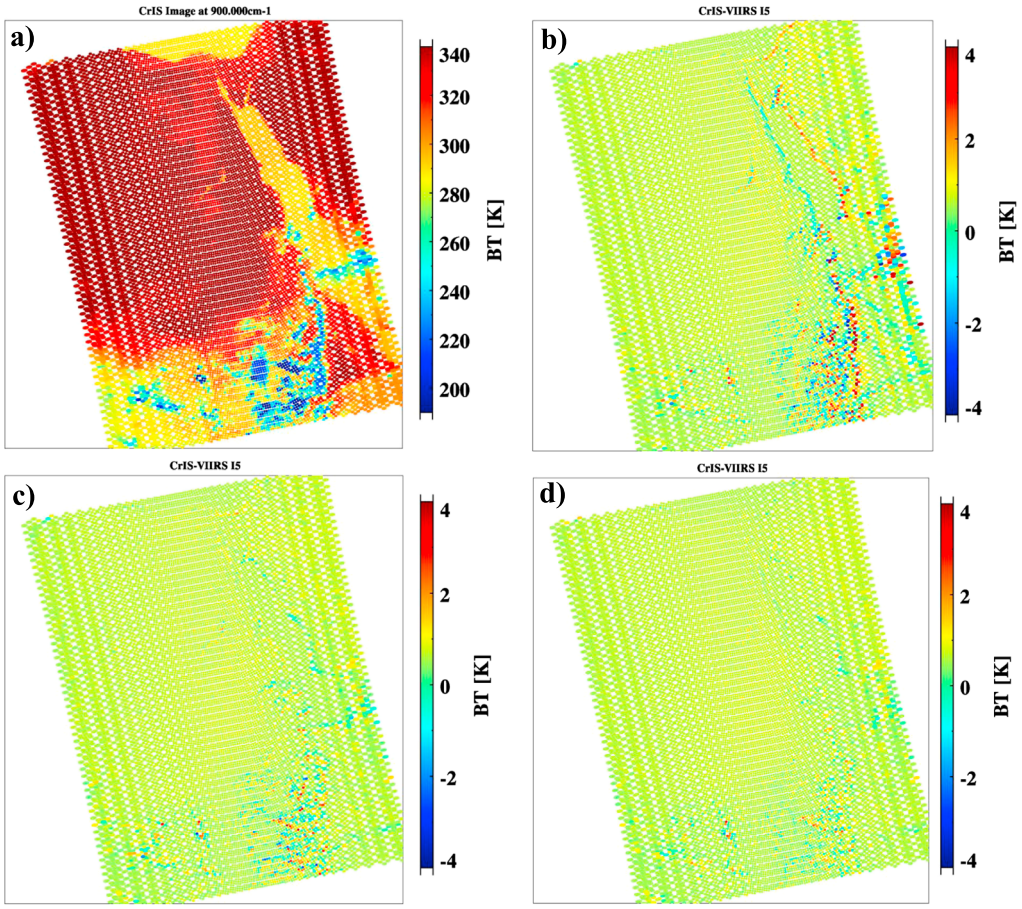

Figure 12. The effects of the updated mapping angles on CrIS geolocation data sets, including (a) CrIS images and CrIS-VIIRS BT difference images from (b) IDPS-produced geolocation data set, (c) ADL-produced geolocation data set with updated cross-track angles, and (d) ADL-produced geolocation data set with both updated cross-track and in-track angles.

which mapping angles are the root causes for CrIS geolocation bias. However, given the assessment results with a total of 2×30 angles, the best strategy is to adjust the 2×30 Scene Selection Mirror (SSM) rotation angles so that it can totally resolve the geolocation error at each scan position.

First, we go through the steps on how the LOS vectors in the SBF frame are derived at each scan position beginning from the detector array. Basically, we begin with the unit vector $\overrightarrow{OA}_{IOAR}$ [1, 0, 0] in the Interferometer Optical Axis Reference (IOAR), which exactly points out from the optical axis of the detector array. Specifically, the following steps are included:

1. Applying rotation on optical axis $\overrightarrow{OA}_{IOAR}$ to get FOV 5 LOS vectors in IOAR using two central FOV offset angles (θ_{IOAR}, $\varnothing_{IOAR}$) in the in-track and cross-track directions. This gives the LOS vector $\overrightarrow{LOS}_{IOAR}$ in IOAR as

$$\overrightarrow{\boldsymbol{LOS}}_{IOAR} = P(\theta_{IOAR})\, Y(\varnothing_{IOAR}) \quad \overrightarrow{\boldsymbol{OA}}_{IOAR}, \tag{9}$$

In equation (9), the alignment of a coordinate system (X_1, Y_1, Z_1) on a second coordinate system (X_2, Y_2, Z_2) are defined by the mapping angles of (ψ, θ, φ) and their transformation matrix $\boldsymbol{T}_{X2Y2Z2/X1Y1Z1}$ can be generally expressed as

$$\boldsymbol{T}_{X2Y2Z2/X1Y1Z1} = R_x(\psi)P_y(\theta)Y_z(\varphi), \tag{10}$$

where the rotation matrices are given by

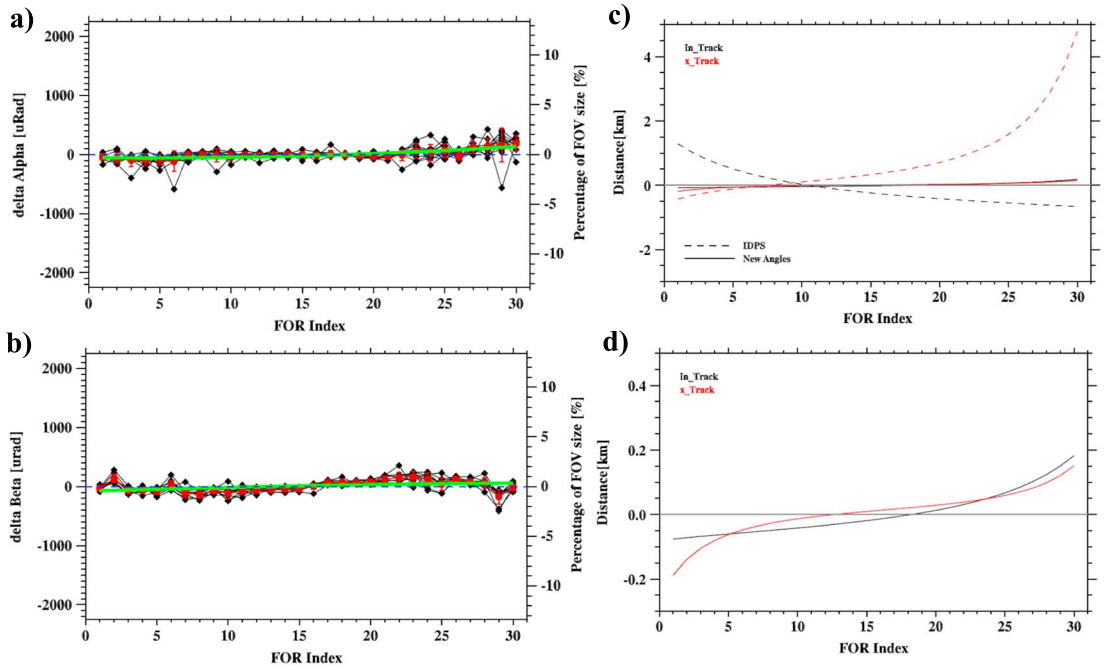

Figure 13. CrIS geolocation assessment results for ADL-reproduced CrIS geolocation data sets with new mapping angles, including (a) the offset angle $\Delta\alpha$ in the in-track direction and (b) $\Delta\beta$ in the cross-track direction, in which the black dots represent the each case's results and the red dots with the error bars that give the statistics including the mean and standard deviation. The green lines indicate the quadratic curve fit line along the scan position. CrIS geolocation assessment results are converted into the distance, which are (c) overlapped with the IDPS results and (d) enlarged.

$$\boldsymbol{R}_X(\psi) = \begin{bmatrix} 1 & 0 & 0 \\ 0 & \cos\psi & -\sin\psi \\ 0 & \sin\psi & \cos\psi \end{bmatrix}, \tag{11}$$

$$\boldsymbol{P}_Y(\theta) = \begin{bmatrix} \cos\theta & 0 & \sin\theta \\ 0 & 1 & 0 \\ -\sin\theta & 0 & \cos\theta \end{bmatrix}, \tag{12}$$

$$\boldsymbol{Y}_Z(\varphi) = \begin{bmatrix} \cos\varphi & -\sin\varphi & 0 \\ \sin\varphi & \cos\varphi & 0 \\ 0 & 0 & 1 \end{bmatrix}. \tag{13}$$

2. Transforming FOV 5 LOS vector from IOAR into Scene Selection Mirror mounting feet Frame (SSMF) using two misalignment angles (θ_{SSMF}, $\varnothing_{SSMF}$) between IOAR and SSMF as

$$\overrightarrow{\boldsymbol{LOS}}_{SSMF} = P(\theta_{SSMF})\, Y(\varnothing_{SSMF})\ \ \overrightarrow{\boldsymbol{LOS}}_{IOAR}. \tag{14}$$

3. Computing the scene selection mirror normal in Scene Selection Mirror mounting feet Frame (SSMF) (fixed coordinate system) by applying rotations from the scan mirror cross-track and in-track angles (a total of 2×30 angles for 30 scan position), which gives

$$\hat{n}^k_{SSM} = P\left(\theta^k_{SSMF}\right) R\left(\psi^k_{SSMF}\right)\, \hat{n}. \tag{15}$$

4. Calculating the reflected FOV LOS vectors using mirror normal in SSMF for each scan position as

$$\overrightarrow{\boldsymbol{LOS}}^k_{SSMF} = \overrightarrow{\boldsymbol{LOS}}_{SSMF} - 2\left(\overrightarrow{\boldsymbol{LOS}}_{SSMF} \cdot \hat{n}^k_{SSM}\right)\hat{n}^k_{SSM}. \tag{16}$$

Note that this step produces a total of 30 LOS vectors and each scan position has its own LOS vector.

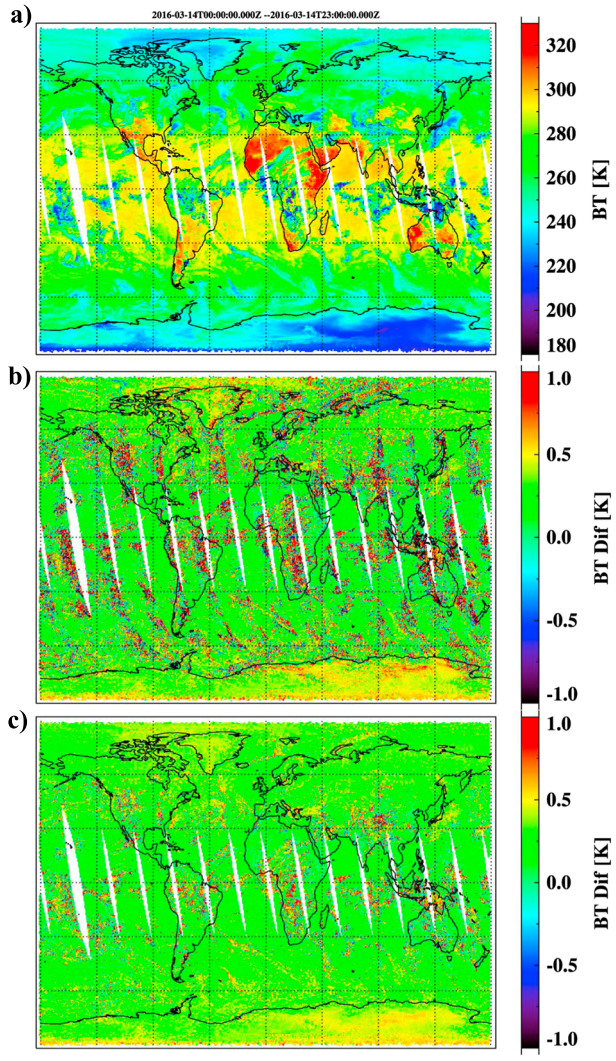

Figure 14. The effects of CrIS geolocation accuracy improvements on CrIS-VIIRS BT differences, including (a) CrIS image at 900 cm^{-1} on 14 March 2016 as well as (b) CrIS-VIIRS BT difference images for original CrIS IDPS geolocation data sets and (c) and reproduced CrIS geolocation data sets with updated mapping angles.

5. Deriving SSMF-to-SBF transformation operator using three angles from SSMF to Scene Selection Module Reference (SSMR), three angles from SSMR to Instrument Alignment Reference (IAR), and three angles from IAR to SBF. This gives

$$\boldsymbol{T}_{SBF/SSMF} = \boldsymbol{T}_{SBF/IAR}\,\boldsymbol{T}_{IAR/SSMR}\boldsymbol{T}_{SSMR/SSMF}. \tag{17}$$

6. Determining CrIS on-axis LOS vectors in SBFs using the SSMF-to-SBF transformation operator. This is determined as

$$\overrightarrow{\boldsymbol{LOS}}^{k}_{SBF} = \boldsymbol{T}_{SBF/SSMF}\,\overrightarrow{\boldsymbol{LOS}}^{k}_{SSMF}. \tag{18}$$

After the above steps, the FOV LOS vectors are expressed in SBF at each scan position, and there are a total of 30 LOS vectors. Following equations (1) and (2), the angles of α_k and β_k can be calculated from each FOV LOS unit vector $\overrightarrow{\boldsymbol{LOS}}^{k}_{SBF}(x_k, y_k, z_k)$ in SBF at scan position k. From the assessment results, we already have the offset angles $\Delta\alpha_k$ and $\Delta\beta_k$. Thus, the true angles of $\alpha_k^{'}$ and $\beta_k^{'}$ that are best matched to VIIRS observations can be computed as

$$\alpha_k^{'} = \alpha_k + \Delta\alpha_k, \tag{19}$$

$$\beta_k^{'} = \beta_k + \Delta\beta_k. \tag{20}$$

Once we have new α and β angles, the new LOS unit vectors that reflect the actual pointing position can be expressed as

$$\overrightarrow{\boldsymbol{LOS}}^{'}_{SBF}\,k = \mathrm{UNIT}\left(z_k\tan\beta_k^{'}, z_k\tan\alpha_k^{'}, z_k\right). \tag{21}$$

So the question is simplified on how to use $\overrightarrow{LOS}_k^{'}$ to retrieve the new set of scan mirror rotation angles in the cross-track and in-track directions. We can use equation (18) to calculate new LOS vector in SSMF $\overrightarrow{\boldsymbol{LOS}}^{'k}_{SSMF}$ as

$$\overrightarrow{\boldsymbol{LOS}}^{'k}_{SSMF} = \boldsymbol{T}^{-1}_{SBF/SSMF}\quad \overrightarrow{\boldsymbol{LOS}}^{'k}_{SBF}, \tag{22}$$

where $\boldsymbol{T}^{-1}_{SBF/SSMF}$ is the inverse SSMF-to-SBF transformation operator.

After that, using equation (16), the new mirror normal $\hat{n}^{'k}_{SSM}$ can be computed as

$$\hat{n}^{'k}_{SSM} = UNIT\left(\overrightarrow{\boldsymbol{LOS}}^{'k}_{SSMF} - \overrightarrow{\boldsymbol{LOS}}_{SSMF}\right). \tag{23}$$

And then, a new set of in-track and cross-track angles can be derived from $\hat{n}^{'k}_{SSM}$ from equation (15), which is shown in Figure 11. It should be pointed out that the angles shown in Figure 11 are computed based on geolocation assessment results of geolocation data set produced from newly updated ADL software (Figure 10)

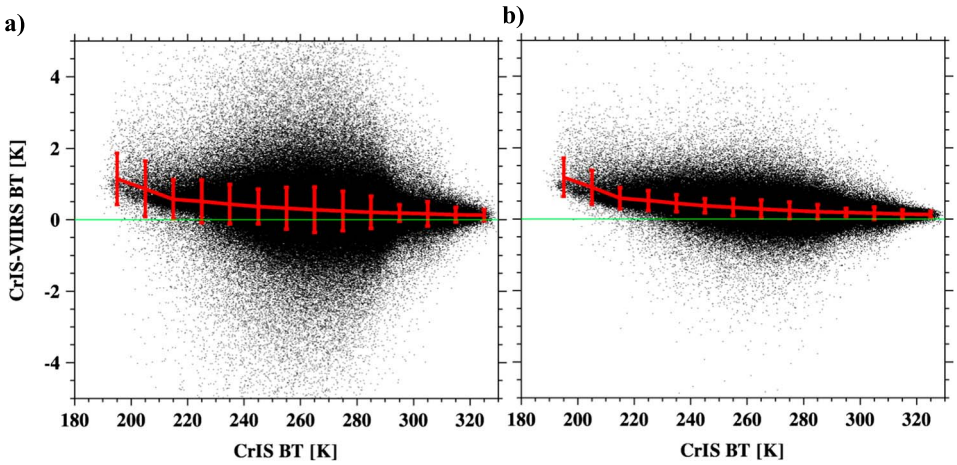

Figure 15. CrIS-VIIRS BT differences versus CrIS BTs for (a) original CrIS IDPS geolocation data sets and (b) reproduced CrIS geolocation data sets with updated mapping angles. The red lines are bin-averaged values with a 10 K interval, while the red bars indicate the standard deviation. Note that the data are only shown in the range from −5 K to 5 K in Figures 15a and 15b.

instead of operational IDPS software (Figures 7 and 8). It shows the angle differences between new angles and old ones can reach up to ~1000 μrad.

4.2. Assessment Results for New Mapping Angles

We replaced old SSM rotation angles with newly derived values in EP and then used ADL with new EP to reproduce the new geolocation data sets. The effects of the updated mapping angles on CrIS geolocation data sets are noticeably shown in Figure 12, which gives CrIS-VIIRS BT difference map in Red Sea region. For original IDPS-produced geolocation data set (Figure 12b), the coastline is obviously noticeable at the end of scan from the CrIS-VIIRS BT difference image, which is due to the geolocation misalignment between CrIS and VIIRS as shown in Figure 9. When using ADL-produced geolocation data sets with updating the SSM mapping angles only in the cross-track direction (Figure 12c), the coastline almost disappears, suggesting that the misalignment between CrIS and VIIRS is dominant by the error in the cross-track direction. Finally, when using ADL-produced geolocation data sets with updating the SSM rotation angles both in the cross-track and in-track directions (Figure 12d), the CrIS-VIIRS BT image is further improved and is hard to see the land features. The three experiments suggest that the newly derived SSM mapping angles have positive impacts on CrIS geolocation accuracy.

The geolocation data sets for the above 10 day data were reproduced using ADL with new mapping angles. These newly produced data are then evaluated using collocated VIIRS, and the final results are given in Figure 13. It clearly indicates significant improvements for the CrIS geolocation data set because the fitting lines (green) in both in-track and cross-track directions are almost along the zero line for all scan positions. On the right plot in Figure 13, it shows the CrIS geolocation accuracy in distance after the mapping angles are updated. The residue error revealed by CrIS is reduced to less than 250 m at the end of the scan. Compared to Figure 10, it is a big improvement.

In the end, to further validate the CrIS geolocation accuracy in different geographic regions, the global CrIS-VIIRS BT difference images on 14 March 2016 are shown in Figure 14 by using the CrIS geolocation data sets with old and updated mapping angles. Before the mapping angles are updated, it clearly shows the large CrIS-VIIRS BT differences at the end of scan almost for every orbit (Figure 14b). However, with newly produced geolocation data sets with updated mapping angles, the CrIS-VIIRS BT differences are greatly reduced globally (Figure 14c). The effects of geolocation improvements are further demonstrated in Figure 15, showing the CrIS-VIIRS BT difference versus CrIS BTs for CrIS for original CrIS IDPS-produced (Figure 15a) and reproduced CrIS geolocation data sets with updated mapping angles (Figure 15b). It indicates that the spread (standard deviations) of CrIS-VIIRS BT differences are reduced with improved geolocation accuracy, while the mean values of CrIS-VIIRS BT differences keep similar values. This suggests that, for intercalibration, the spatial mismatch between two sensors mostly impacts on the intercalibration uncertainties. In order to

precisely characterize their radiometric differences, either enough samplings or homogeneous scenes are needed to beat down the uncertainties [*Tobin et al*., 2016]. Overall, this implies that improvements of CrIS geolocation will benefit the application that needs combination of CrIS and VIIRS data for geophysical retrievals, quality control for data assimilation, and intersensor calibration.

5. Conclusion

The data quality of geolocated, radiometrically, and spectrally calibrated radiances with annotated quality indicators from CrIS are important for geophysical parameter retrievals and data assimilations that need CrIS radiances as inputs. This paper improves the method by *Wang et al*. [2013] and presents an improved scheme for CrIS geolocation assessment for all scan angles based on CrIS line-of-sight (LOS) vectors. More importantly, the new method is capable of performing postlaunch on-orbit geometric calibration by optimizing mapping angle parameters based on assessment results and thus can be further extended to the following CrIS sensors on JPSS-1 and JPSS-2. The basic idea is to find the best collocation position between VIIRS and CrIS measurements by perturbing CrIS LOS vector in the cross-track and in-track directions with small-step angles. The offset angles at the best collocation position between CrIS and VIIRS are then used to evaluate the CrIS geolocation accuracy.

The proposed method is then employed to evaluate the SNPP CrIS geolocation accuracy. The error characteristics are revealed along the scan positions in the cross-track and in-track directions. It is found that there is relatively large error (~4 km) in the cross-track direction relative to VIIRS at the end of scan. With newly updated mapping angles, the geolocation accuracy is greatly improved for all scan positions (less than 0.3 km). This makes CrIS and VIIRS align together and benefits the application that needs combination of CrIS and VIIRS measurements and products.

As a final note, we like to point out that the method proposed in this study lays down the frame work using high spatial imager measurements to assess the geolocation accuracy of sounder instruments. It can be further extended to other infrared and microwave sounders (such as the Advanced Technology Microwave Sounder) in the future.

Acknowledgments

The VIIRS I5 SDR data and CrIS SDR and RDR data for this paper can be downloaded at NOAA's Comprehensive Large Array Data Stewardship System at http://www.class.ncdc.noaa.gov/. The authors thank the anonymous reviewers for providing valuable comments for the study. This study is funded by the NOAA JPSS Program Office. The authors thank Mark Esplin of Utah State University from NOAA, David Johnson from NASA Langley Research Center, Joe Predina from Logistikos Engineering LLC, and the CrIS Team in Harris for providing valuable comments and discussion. Likun Wang is supported by NOAA grant NA14NES4320003 (Cooperative Institute for Climate and Satellites) at the University of Maryland/ESSIC. The manuscript contents are solely the opinions of the authors and do not constitute a statement of policy, decision, or position on behalf of NOAA or the U.S. government.

References

Bangert, J., W. Puatua, G. Kaplan, J. Bartlett, W. Harris, A. Fredericks, and A. Monet (2011), *User's Guide to NOVAS Version C3.1*, U.S. Nav. Obs, Washington, D. C.

Black, H. (1964), A passive system for determining the attitude of a satellite, *AIAA J.*, *2*(7), 1350–1351, doi:10.2514/3.2555.

Brunel, P., and P. Roquet (2015), VIIRS-CrIS mapping, in *2015 CSPP/IMAPP Users' Group Meeting*, Darmstadt, Germany. [Available at http://www.ssec.wisc.edu/meetings/cspp/2015/Agenda%20PDF/Wednesday/Brunel_cspp_darmstatd_avril_2015.pdf.]

Divakarla, M., et al. (2014), The CrIMSS EDR algorithm: Characterization, optimization, and validation, *J. Geophys. Res. Atmos.*, *119*, 4953–4977, doi:10.1002/2013JD020438.

Eresmaa, R. (2014), Imager-assisted cloud detection for assimilation of Infrared Atmospheric Sounding Interferometer radiances, *Q. J. R. Meteorol. Soc.*, *140*(684), 2342–2352, doi:10.1002/qj.2304.

Eresmaa, R., A. P. McNally, and N. Bormann (2014), Assimilation of Cross-track Infrared Sounder radiances at ECMWF, paper presented at The 19th International TOVS Study Conference, Jeju Island, South Korea, 26 March–1 April, 2014.

Han, Y., et al. (2013), Suomi NPP CrIS measurements, sensor data record algorithm, calibration and validation activities, and record data quality, *J. Geophys. Res. Atmos.*, *118*, 12,734–12,748, doi:10.1002/2013JD020344.

JPSS Configuration Management Office (2011a), *Joint Polar Satellite System (JPPS) VIIRS Geolocation Algorithm Theoretical Basis Document (ATBD)*. [Available at https://www.star.nesdis.noaa.gov/smcd/spb/nsun/snpp/VIIRS/ATBD-VIIRS-Geolocation_20131212.pdf.]

JPSS Configuration Management Office (2011b), *Joint Polar Satellite System (JPSS) Cross Track Infrared Sounder (CrIS) Sensor Data Records (SDR) Algorithm Theoretical Basis Document (ATBD)*. [Available at https://www.star.nesdis.noaa.gov/jpss/documents/ATBD/D0001-M01-S01-002_JPSS_ATBD_CrIS-SDR_C.pdf.]

JPSS Configuration Management Office (2013), *Joint Polar Satellite System (JPSS) Algorithm Theoretical Basis Document for the Cross Track Infrared Sounder (CrIS)*, vol. II, *Environ. Data Records, Revis. B*. [Available at https://www.star.nesdis.noaa.gov/jpss/documents/ATBD/D0001-M01-S01-007_JPSS_ATBD_CrIMSS_B.pdf.]

Li, J., W. P. Menzel, F. Sun, T. J. Schmit, and J. Gurka (2004), AIRS subpixel cloud characterization using MODIS cloud products, *J. Appl. Meteorol.*, *43*(8), 1083–1094.

Nalli, N. R., et al. (2013), Validation of satellite sounder environmental data records: Application to the Cross-track Infrared Microwave Sounder Suite, *J. Geophys. Res. Atmos.*, *118*, 13,628–13,643, doi:10.1002/2013JD020436.

Shephard, M. W., and K. E. Cady-Pereira (2015), Cross-track Infrared Sounder (CrIS) satellite observations of tropospheric ammonia, *Atmos. Meas. Tech.*, *8*(3), 1323–1336, doi:10.5194/amt-8-1323-2015.

Strow, L. L., H. Motteler, D. Tobin, H. Revercomb, S. Hannon, H. Buijs, J. Predina, L. Suwinski, and R. Glumb (2013), Spectral calibration and validation of the Cross-track Infrared Sounder on the Suomi NPP satellite, *J. Geophys. Res. Atmos.*, *118*, 12,486–12,496, doi:10.1002/2013JD020480.

Tobin, D., et al. (2013), Suomi-NPP CrIS radiometric calibration uncertainty, *J. Geophys. Res. Atmos.*, *118*, 10,589–10,600, doi:10.1002/jgrd.50809.

Tobin, D., R. Holz, F. Nagle, and H. Revercomb (2016), Characterization of the Climate Absolute Radiance and Refractivity Observatory (CLARREO) ability to serve as an infrared satellite intercalibration reference, *J. Geophys. Res. Atmos.*, *121*, 4258–4271, doi:10.1002/2016JD024770.

Wang, L., Y. Han, D. Tremblay, F. Weng, and M. Goldberg (2012), Inter-comparison of NPP/CrIS radiances with VIIRS, AIRS, and IASI: A post-launch calibration assessment, in *Earth Observing Missions and Sensors: Development, Implementation, and Characterization II*, vol. 8528, edited by H. Shimoda et al., Bellingham, Wash.

Wang, L., D. A. Tremblay, Y. Han, M. Esplin, D. E. Hagan, J. Predina, L. Suwinski, X. Jin, and Y. Chen (2013), Geolocation assessment for CrIS sensor data records, *J. Geophys. Res. Atmos.*, *118*, 12,690–12,704, doi:10.1002/2013JD020376.

Wang, L., Y. Chen, and Y. Han (2016a), Impacts of field of view configuration of Cross-track Infrared Sounder on clear-sky observations, *Appl. Opt.*, *55*(25), 7113–7119, doi:10.1364/AO.55.007113.

Wang, L., D. Tremblay, B. Zhang, and Y. Han (2016b), Fast and accurate collocation of the visible infrared imaging radiometer suite measurements with Cross-Track Infrared Sounder, *Remote Sens.*, *8*(1), 76, doi:10.3390/rs8010076.

Weng, F., L. Zhou, and K. Carey (2016), JPSS life-cycle data reprocessing for advancing weather and climate applications, in *21st Conference on Satellite Meteorology*, Madison, Wis. [Available at https://ams.confex.com/ams/21SATMET20ASI/webprogram/Paper297223.html.]

Wolfe, R. E., G. Lin, M. Nishihama, K. P. Tewari, J. C. Tilton, and A. R. Isaacman (2013), Suomi NPP VIIRS prelaunch and on-orbit geometric calibration and characterization, *J. Geophys. Res. Atmos.*, *118*, 11,508–11,521, doi:10.1002/jgrd.50873.

Zavyalov, V., et al. (2013), Noise performance of the CrIS instrument, *J. Geophys. Res. Atmos.*, *118*, 13,108–13,120, doi:10.1002/2013JD020457.